

# COSMOS-Web galaxy groups: Evolution of red sequence and quiescent galaxy fraction

Greta Toni<sup>1,2,3\*</sup>, Matteo Maturi<sup>3,4</sup>, Gianluca Castignani<sup>2</sup>, Lauro Moscardini<sup>1,2,5</sup>, Ghassem Gozaliasl<sup>6,7</sup>, Alexis Finoguenov<sup>7</sup>, Sina Taamoli<sup>8</sup>, Hollis B. Akins<sup>9</sup>, Rafael C. Arango-Toro<sup>10</sup>, Caitlin M. Casey<sup>11,12</sup>, Nicole E. Drakos<sup>13</sup>, Andreas L. Faisst<sup>14</sup>, Carter Flayhart<sup>15</sup>, Maximilien Franco<sup>16</sup>, Fabrizio Gentile<sup>16,2</sup>, Ali Hadi<sup>8</sup>, Santosh Harish<sup>15</sup>, Hossein Hatamnia<sup>8</sup>, Olivier Ilbert<sup>10</sup>, Shuowen Jin<sup>12,17</sup>, Jeyhan S. Kartaltepe<sup>15</sup>, Ali Ahmad Khostovan<sup>18,15</sup>, Anton M. Koekemoer<sup>19</sup>, Gavin Leroy<sup>20</sup>, Georgios E. Magdis<sup>12,17,21</sup>, Henry Joy McCracken<sup>22</sup>, Jed McKinney<sup>9</sup>, Louise Paquereau<sup>22</sup>, Jason Rhodes<sup>23</sup>, R. Michael Rich<sup>24</sup>, Brant E. Robertson<sup>25</sup>, Rasha M. Samir<sup>26</sup>, Diana Scognamiglio<sup>27</sup>, Samaneh Shamyati<sup>8</sup>, Marko Shuntov<sup>12,21,28</sup>, and Jorge A. Zavala<sup>29</sup>

(Affiliations can be found after the references)

September 11, 2025

## ABSTRACT

**Aims.** We investigate the redshift evolution and group richness dependence of the quiescent galaxy fraction and red-sequence parameters in COSMOS galaxy groups, spanning a wide redshift range, from  $z = 0$  to  $z = 3.7$ .

**Methods.** We analyzed the deep and well-characterized sample of groups recently detected with the AMICO algorithm in the COSMOS(-Web) field. Our study of the quiescent galaxy population is based on a machine-learning classification tool based on rest-frame magnitudes. The algorithm learns from several traditional methods to estimate the probability of a galaxy being quiescent, achieving high precision and recall. Starting from this classification, we computed quiescent galaxy fractions within groups via two methods: one based on the membership probabilities provided by AMICO, which rely on an analytical model, and another using a model-independent technique. We then detected the red sequence (RS) by estimating the ridgeline position using probability-weighted photometric data, followed by sigma clipping to remove outliers. This analysis was performed using both rest-frame magnitudes and observed-frame magnitudes with rest-frame matching. We compared the results from both approaches and investigated the redshift and richness dependence of the RS parameters.

**Results.** We found that the quiescent galaxy population in groups builds up steadily from  $z = 1.5 - 2$  across all richnesses, with faster and earlier growth in the richest groups. The first galaxies settle onto the RS ridgeline by  $z \sim 2$ , consistent with current evolutionary scenarios. Notably, we reported a rare overdensity of quiescent galaxies at  $z = 3.4$ , potentially one of the most distant early red sequences observed. Extending our study to X-ray properties, we found that X-ray faint groups have, on average, lower quiescent fractions than X-ray bright ones, likely reflecting their typical location in filaments where pre-processing is lower. Leveraging the broad wavelength coverage of COSMOS2025, we traced RS evolution using observed and rest-frame colors over  $\sim 12$  Gyr, finding no significant trends in either slope or scatter of the ridgeline.

**Key words.** galaxies: clusters: general – galaxies: evolution – galaxies: groups: general – galaxies: star formation – galaxies: high-redshift – large-scale structure of Universe

## 1. Introduction

Dense environments typically host galaxy populations characterized by lower star-formation rates (SFRs), and redder stellar populations compared to lower-density environments, at least up to  $z \sim 1$ . This environmental segregation is reflected in the well-known SFR (or morphology)-density relation (e.g. Dressler 1980; Balogh et al. 1998). The way galaxies transform is generally explained as the result of a strongly intertwined impact of intrinsic properties, like stellar mass (*nature*) and factors related to the different environment galaxies experience in their lifetimes (*nurture*) (e.g. De Lucia et al. 2012). The disentanglement of mass- and environment-driven quenching remains debated. Building on the pioneering work of Peng et al. (2010) establishing this two-channel framework, recent studies (e.g. Chartab et al. 2020; Taamoli et al. 2024; Zheng et al. 2025) have expanded this view, showing that mass quenching is a strong driver across all cosmic times especially on very massive galaxies, while environmental quenching dominates the quenching of galaxies in dense environments at later epochs and especially for

satellites, generating a population of quiescent, red, passively evolving galaxies. This population, hosted in dense environments like clusters and groups, is known to occupy a tight grouping in the color-magnitude diagram (CMD), known as the red sequence (RS). The study of this prominent feature in the CMDs of galaxy clusters and groups is crucial for tracing the formation and evolution of quiescent galaxies across cosmic time. The red sequence is thought to reflect the combined effect of star formation history, chemical enrichment, and environmental quenching, which can be explored by studying the parameters of the RS ridgeline. The slope of the line reflects the mass-metallicity relation, the color scatter, and the rest-frame zero-point (or the observed average color) indicate the galaxy population mass and star-formation history (e.g. Kodama & Arimoto 1997). The red sequence and quiescent fraction have been extensively studied in massive clusters (e.g. Mei et al. 2009; Stott et al. 2009; Hennig et al. 2017). However, characterizing them in galaxy groups — which dominate the halo mass function and host the bulk of galaxies in the Universe — can provide deeper insights into the different quenching processes and galaxy formation scenarios.

\* e-mail: greta.toni4@unibo.it

Over the past years, the presence of a well-defined red sequence in clusters and groups has also been used as a tracer to identify these systems and create robust catalogs up to  $z \sim 1$  (e.g. Gladders & Yee 2000; Rykoff et al. 2014, 2016). While red fractions and RS properties have been well characterized in the local universe and up to intermediate redshifts ( $z \sim 1$ ; e.g. Menci et al. 2008; Rudnick et al. 2009; Fritz et al. 2014), a better understanding of how the first galaxies quenched and built up the red sequence can be addressed by studying samples of groups and clusters at higher redshifts, up to the earlier stages of cluster formation ( $z > 1.5 - 2$ ; e.g. Kravtsov & Borgani 2012; Shimakawa et al. 2018). This epoch reveals a diversity in galaxy populations, with systems showing enhanced star formation, Active Galactic Nuclei (AGN) activity, and merging activity (e.g. Brodwin et al. 2013; Alberts et al. 2016; Wang et al. 2016), and others (sometimes even coexisting) with an early-phase red sequence and high red fractions, especially in the central regions of galaxy overdensities (e.g. Andreon & Huertas-Company 2011; Spitler et al. 2012; Strazzullo et al. 2013, 2016; Zavala et al. 2019).

The James Webb Space Telescope (JWST) has recently demonstrated its unique power to detect quiescent galaxies at high redshift and to probe their environments (e.g. Jin et al. 2024; Ito et al. 2025; de Graaff et al. 2025). In this work, we aim to characterize red fractions and red sequence in groups and low-mass clusters, across  $\sim 12$  Gyrs of cosmic history. To do so, we leverage our recent work in building the COSMOS-Web (Casey et al. 2023) group sample (Toni et al. 2025): the largest group catalog based on deep JWST observations to date, spanning  $z = 0.08$  to  $z = 3.7$ . In this catalog, galaxy groups have been detected with the Adaptive Matched Identifier of Clustered Objects (AMICO; Bellagamba et al. 2018; Maturi et al. 2019). The AMICO algorithm, officially selected for cluster detection in Euclid (Euclid Collaboration: Adam et al. 2019), is based on optimal linear matched filtering, and has been proven to be a flexible tool for identifying groups and even protocluster cores (or overdensity peaks) up to  $z \sim 4$  and down to less than  $10^{13} M_{\odot}$  (Toni et al. 2024, 2025). What is particularly interesting for this analysis is that AMICO does not make explicit use of colors, limiting the possibility of biasing the selection towards systems with a clear red sequence, which is crucial when we want to study its build-up process and the diversity in the galaxy population that clusters and groups show, for instance, at  $z \gtrsim 1 - 1.5$ . In this study, we also analyzed the first AMICO catalog generated on the COSMOS field (Scoville et al. 2007) to explore the relationship between our results and the group X-ray emission. The sample covers a  $\sim 3$  times larger area (the full COSMOS field) up to  $z = 2$  and includes mass estimates and X-ray properties of optically-selected groups (Toni et al. 2024).

The paper is organized as follows. Section 2 introduces the COSMOS group catalogs created with AMICO and the underlying galaxy catalogs. In Sect. 3, we describe our machine learning method for classifying galaxies as quiescent or star-forming, including training, algorithm testing, and performance comparison. Section 4 analyzes the evolution of quiescent fractions in COSMOS groups and their dependence on group properties. Section 5 characterizes the red sequence in our sample and compares it with evolutionary synthesis models. Finally, Sect. 6 summarizes the main results and outlines future developments. In our analysis, we assume a standard concordance flat  $\Lambda$ CDM cosmology with  $\Omega_m = 0.3$ ,  $\Omega_{\Lambda} = 0.7$ , and  $h = H_0 / (100 \text{ km/s/Mpc}) = 0.7$ . Magnitudes are expressed in the AB system and corrected for Galactic extinction.

## 2. The catalog of galaxies and galaxy groups

The COSMOS field (Scoville et al. 2007) is one of the most data-rich extragalactic regions, and benefits from extensive multi-wavelength coverage from X-ray to radio (e.g., Hasinger et al. 2007; Civano et al. 2016; Smolčić et al. 2017). Optical imaging encompasses coverage from several instruments, including the Canada-France-Hawaii Telescope (Sawicki et al. 2019), the Subaru Suprime-Cam (Taniguchi et al. 2015), the high-resolution Hubble Space Telescope ACS data (Koekemoer et al. 2007), and the broadband data in the  $g$ ,  $r$ ,  $i$ ,  $z$ , and  $y$  filters from the Subaru Hyper Suprime-Cam (Aihara et al. 2022). Near-infrared coverage from the UltraVISTA survey (McCracken et al. 2012; Moneti et al. 2023) further complements this extensive dataset.

Building on this legacy, the COSMOS-Web Survey (PIs: Kartaltepe and Casey; Casey et al. 2023) is a JWST Cycle 1 program covering  $0.54 \text{ deg}^2$  with four filters F115W, F150W, F277W, and F444W in NIRCcam (Rieke et al. 2023; Franco et al. 2025), achieving  $5\sigma$  point-source depths of 27.5–28.2 mag. These filters offer a coverage of the near-infrared regime that is highly complementary to the UltraVISTA survey filters. An additional non-contiguous area is observed with the F770W MIRI filter (Wright et al. 2022; Harish et al. 2025).

The COSMOS-Web photometric galaxy catalog (also known as COSMOS2025; Shuntov et al. 2025), specifically targets the JWST-imaged region, building on previous COSMOS catalogs like COSMOS2009 (Ilbert et al. 2009), COSMOS2015 (Laigle et al. 2016), and COSMOS2020, (Weaver et al. 2022), and includes over 784,000 sources.

The COSMOS2025 catalog sources were detected using a PSF-homogenized  $\chi^2$  image combining all NIRCcam bands, using SourceXtractor++ (Bertin et al. 2022) to address PSF variations across datasets, boasting high spatial resolution reflected in the deblending power of the source extraction. In the COSMOS2025 catalog, redshifts (and all physical properties) are derived using the LePhare template-fitting code (Arnouts et al. 2002; Ilbert et al. 2006) with an expanded set of templates based on Bruzual & Charlot (2003) models (Ilbert et al. 2015). When compared to high-confidence spectroscopic samples, the photometric redshifts achieve a precision of  $\sim 0.01$  for bright galaxies ( $m_{F444W} < 23$ ) with  $< 2\%$  catastrophic outliers, and maintain  $< 0.03$  precision with  $\sim 10\%$  outliers even for  $26 < m_{F444W} < 28$ . When divided between quiescent and star-forming, according to the NUVrJ criterion (Ilbert et al. 2013), galaxy photo- $z$ s achieve 0.008 and 0.013 precision, and 2.26% and 1.95% outliers, respectively (see Table 3 in Shuntov et al. 2025).

We based our analysis on the new COSMOS-Web group catalog, presented in Toni et al. (2025) and extending up to  $z = 3.7$  (the COSMOS-Web group catalog, hereinafter). The candidate groups were detected using the AMICO algorithm (Bellagamba et al. 2011, 2018; Maturi et al. 2019).

AMICO is a linear optimal matched filter that detects clusters and groups in photometric galaxy catalogs using the galaxy position, photometric redshift, and an additional galaxy property (in the simplest case), such as the magnitude in a reference band. The filtering process produces an estimate of the cluster amplitude for each pixel of the analyzed three-dimensional space of sky coordinates and redshifts. Then, it selects the candidates at the peaks in the amplitude map with the highest signal-to-noise ratio ( $S/N$ ). After each selection, it assigns member galaxies to the cluster/group candidate by attributing a membership probability that depends on the galaxy properties, i.e., the magnitude and the redshift. Finally, AMICO uses this information to remove the signal of the detected object from the map, allowing

easier detection of blended systems (for details, see [Bellagamba et al. 2018](#); [Maturi et al. 2019](#)). Each AMICO run returns a list of candidates with their respective lists of member galaxies, each with its association probability.

The COSMOS-Web group catalog was retrieved by applying AMICO to COSMOS2025. The group search was performed using the galaxy position, photo- $z$  distribution, and magnitude in a reference band, the NIRCам F150W band, extending to magnitude 27.3, making it the deepest AMICO application to date. The catalog includes 1678 group and protocluster core candidates in the COSMOS-Web field up to  $z = 3.7$ , with  $S/N > 6.0$ , and richness ( $\lambda_*$ ) cut at a minimum value of 2 and reaching up to  $\sim 80$ . More than 500 groups have their redshift confirmed by assigning spectroscopic counterparts ([Toni et al. 2025](#)).

In this study, we also include an analysis of our first COSMOS catalog, AMICO-COSMOS ([Toni et al. 2024](#)), to explore the relation with group X-ray emission. Unlike COSMOS-Web, AMICO-COSMOS was built by applying the AMICO algorithm to the COSMOS2020 (and 2015) catalog (covering the full COSMOS field). This group search was tested with three different photometric bands. The catalog boasts the availability of associated X-ray properties, like luminosity, flux, and mass, for over 600 candidate groups and clusters.

### 3. Classification of galaxies with machine learning

Since the AMICO galaxy group catalogs are based on input photometric galaxy catalogs in the COSMOS field, our goal is to classify COSMOS galaxies. Several methods have been developed over the past years to select quiescent and star-forming galaxies (see e.g. [Pearson et al. 2023](#), for an overview), spanning from a classic sharp cut in sSFR ([Salim et al. 2018](#)), to color selections (e.g. [Whitaker et al. 2011](#); [Ilbert et al. 2013](#)) and the use of spectroscopic features (e.g. [Baldwin et al. 1981](#); [Gallazzi et al. 2014](#)). In this work, in order to classify galaxies into quiescent (red) and star-forming (blue), we used a new approach that incorporates the information from several "classical" methods to train a machine learning (ML) model. We chose to test two algorithms, one non-linear and one linear: the eXtremeGradientBoosting classifier (XGB; [Chen & Guestrin 2016](#)) and the LinearDiscriminantAnalysis classifier (LDA; [Fisher 1936](#)), both as implemented in scikit-learn Python package ([Pedregosa et al. 2011](#)).

#### 3.1. Machine learning algorithms

The XGB algorithm belongs to the class of gradient boosted trees ([Friedman 2000](#)). It classifies data by building decision trees sequentially, where each new tree corrects the errors of the previous ones using gradient descent optimization. This algorithm is well-suited for classification tasks on structured data, offering high predictive accuracy, built-in handling of missing values, and regularization to mitigate overfitting. It also includes parameters to effectively handle unbalanced class distributions. Compared to linear classification methods, it can model complex, non-linear relationships more effectively, despite being more computationally expensive and based on more complex modeling.

The LDA algorithm classifies data using linear combinations of features, assuming that targets in classes are normally distributed. This makes it a simple and efficient classification method, especially for small datasets for which these assumptions hold. However, it is less flexible than non-linear methods like XGB, less efficient with complex patterns, and does not include a default handling of unbalanced classes or missing values.

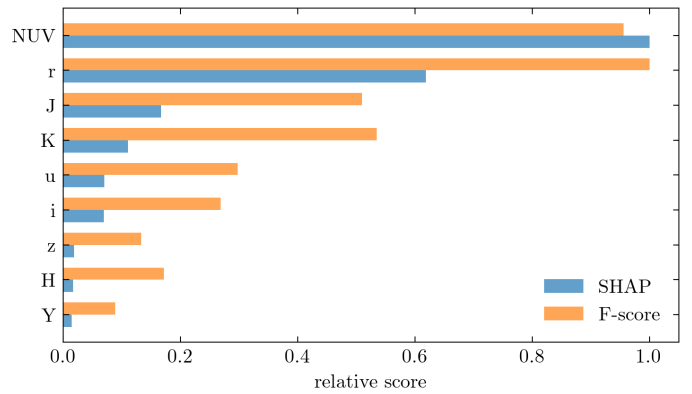


**Fig. 1.** Feature importance for an initial XGB training, measured by the F-score (relative split frequency; orange bars), highlights bands directly used to define ground-truth labels are the most frequent in decision splits. To better assess feature impact, we evaluate SHAP scores ([Lundberg & Lee 2017](#)), which quantify the relative feature contribution to predictions (blue bars). Both approaches confirm that rest-frame magnitudes in  $r$ ,  $NUV$ ,  $K$  and  $J$  provide the strongest constraining power.

For this application, we are dealing with highly unbalanced data, since photometric galaxy catalogs are expected to contain many more examples of blue star-forming galaxies rather than red elliptical galaxies. In the classification problem, these two are therefore referred to as the majority and minority classes, respectively. Class imbalance can be mitigated through the generation of synthetic data. One of the most used methods for data generation is the Synthetic Minority Over-sampling Technique (SMOTE; [Chawla et al. 2011](#)), which creates additional examples for the minority class via feature interpolation between existing data. This generally helps improve decision boundaries and reduces bias towards the majority class. We tested the classification with LDA both with and without the generation of synthetic data. The LDA method also requires the data to be scaled and normalized before training, which was done with the StandardScaler method from scikit-learn.

#### 3.2. Training and testing set

We chose to train and test the ML models on a galaxy sample based on the COSMOS2015 galaxy catalog ([Laigle et al. 2016](#)). Choosing this sample ensures a realistic representation of the features and properties of the galaxies that we want to classify. We chose not to train the algorithm on a subsample of COSMOS2025 since we aim to explore the full sample without compromising statistics and without introducing the risk of repeated data points in the training and target set, which may lead to overfitting. By choosing COSMOS2015 as the training set, we have no data-point overlap with the target dataset.

The first step to create a training/testing set is to clean the catalog to reduce the possibility of training the models on misclassified or spurious objects. For this reason, we performed a conservative cleaning applying the following cuts:

- we removed stars ( $\text{type}=1$ ) and unclassified objects due to SED fitting failure;
- we selected only data with high quality photometry according to the SExtractor flagging system in optical broad bands and UltraVISTA bands:  $[\text{BAND}]_{\text{FLAGS}} < 4$ ;
- we removed masked objects, by applying the AMICO-COSMOS visibility mask and by filtering for  $\text{FLAG\_PETER}$



in  $(0, 4, 6)$  (for details on this selection, see [Toni et al. 2024](#));

- we removed galaxies located within 0.05 degrees from pairs of bright star halo (or halo-border pair), resulting in a more conservative mask where the field is more fragmented;
- finally, we cut the dataset at  $H < 25$  (mode of the magnitude distribution) to discard faint sources with large magnitude errors and homogenize completeness.

This cleaning yielded a sample of around 300,000 galaxies in our training and testing set. In order to establish the "ground truth" in the classification of galaxies for the training/testing set, we used the classification label yielded by several classical methods. We proceeded as follows. First, we selected four classical methods widely used in the literature to discriminate between the two galaxy classes:

- NUVrJ ([Ilbert et al. 2013](#)): a rest-frame color-color cut at  $NUV - r = 3(r - J) + 1$  and  $NUV - r = 3.1$ ;
- sSFR threshold ([Salim et al. 2018](#)): a fixed cut in sSFR at  $10^{-10.5} \text{ yr}^{-1}$ , as adopted for instance by [Euclid Collaboration: Humphrey et al. \(2023\)](#) and [Bisigello et al. \(2020\)](#);
- Sa-color evolution ([Andreon 2006](#); [Radovich et al. 2020](#)): a cut given by the evolution in  $z$  of the observed color of a modeled Sa-type galaxy. Colors bracket the 4000 Å break;
- NUVrK ([Davidzon et al. 2016](#)): a rest-frame color-color cut at  $NUV - r = 1.37(r - K) + 2.6$  and  $NUV - r = 3.15$  and  $r - K = 1.3$ .

We classified galaxies into three categories according to these four methods: the galaxy is flagged as quiescent if it satisfies most of the four criteria (7% of the sample). The same procedure is followed to classify star-forming galaxies (92% of the sample). If the classification is ambiguous (e.g. 2 vs 2), the galaxy is stored in the third class. This third class allows us to identify galaxies with the following characteristics: those with uncertain classifications, because of missing UV photometry and/or ambiguous SED fitting, as well as those in a physical transition phase between the red sequence and the blue cloud, a regime commonly referred to as the green valley. This category of objects represents  $\sim 1\%$  of the full sample. Given the small statistics, it could not be introduced as a third class in the learning process and the classification. Therefore, we decided to remove these objects from the training and testing sets. This reduces ambiguity in the classification and results in an improvement of the performances we describe in Sect. 3.4 of about 2–5% in all evaluation metrics for the minority class. The final selected sample is then randomly divided into training (2/3) and testing set (1/3) using the `scikit-learn train_test_split` function.

### 3.3. Feature engineering

Feature engineering is the ML pre-processing step of selecting, evaluating, and adjusting features, including the handling of missing data, so that the ML model can better capture patterns in the data. First of all, we selected all rest-frame magnitudes available in both COSMOS2015 and COSMOS2020. These are the magnitudes in the following bands:  $NUV$ ,  $u$ ,  $r$ ,  $i$ ,  $z$ ,  $Y$ ,  $J$ ,  $H$  and  $K$ . To get an estimate of the impact of features on the decision-making process, we performed an initial training with the XGB algorithm, which easily allows the evaluation of feature importance. The results are shown in Fig. 1. The importance is measured in terms of the F-score (or weight), which is the number of times a feature appears in the decision tree splitting. The  $r$ ,  $NUV$ ,  $J$ , and  $K$  bands are the most frequent features used in

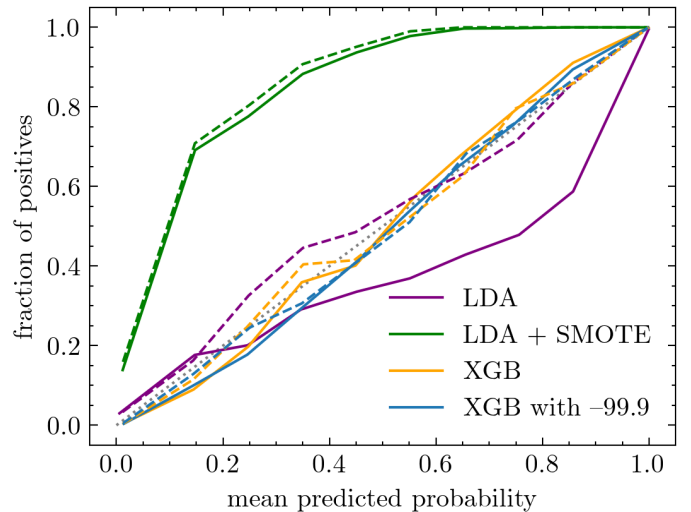


**Fig. 2.** Calibration curves showing the bias between predicted probability and fraction of positives (star-forming galaxies) using all rest-frame magnitude bands (solid lines) and the four most impacting in the decision (dashed line). Different colors represent different methods and configurations, as in the legend.

the decision-making process. This result is expected, as these bands are directly used in assigning the ground-truth labels. To gain deeper insight into feature impact, we also evaluated the SHAP score ([Lundberg & Lee 2017](#)), which indicates how much each feature contributes to the model's predictions. The rest-frame magnitudes in  $r$ ,  $NUV$ ,  $J$ , and  $K$  are confirmed as the features with the greatest constraining power in the model predictions. These 4 magnitude bands are also the only rest-frame magnitudes available in the current release of the COSMOS2025 galaxy catalog at the moment of writing. Since the selection of features is not trivial, and often a few features with high importance simplify the model and lead to better performance than a large number of features, we chose to test and compare results using all magnitudes and with only the best-ranked 4. In Sect. 3.4, we describe the differences in performance depending on the set of chosen features in more detail.

The XGB algorithm is sparsity-aware, meaning it can naturally handle missing data. In our application, this is particularly useful at high redshift or in regions with poor photometry, as it allows us to include galaxies that are missing some rest-frame magnitudes rather than discarding them. Missing values are imputed with an arbitrary constant ( $-99.9$ ), chosen to be clearly distinguishable from real values. Because XGB does not create artifacts from such artificial flags, this strategy is effective; indeed, [Euclid Collaboration: Humphrey et al. \(2023\)](#) showed that using a flagging number, like  $-99.9$ , outperforms other imputation methods such as mean, median, or minimum. This approach enables the algorithm to learn from both fully and partially characterized galaxies. We tested the XGB algorithm with and without imputation of a constant value to recover missing data.

### 3.4. Results

To evaluate the algorithms and configurations, we rely on the standard metric used to evaluate classification performance against the testing set: precision, recall, and F1-score. Precision ( $P$ ) is the fraction of correctly identified objects among all objects assigned to a class, analogous to purity in astronomical samples. Recall ( $R$ ) is the fraction of true objects correctly iden-

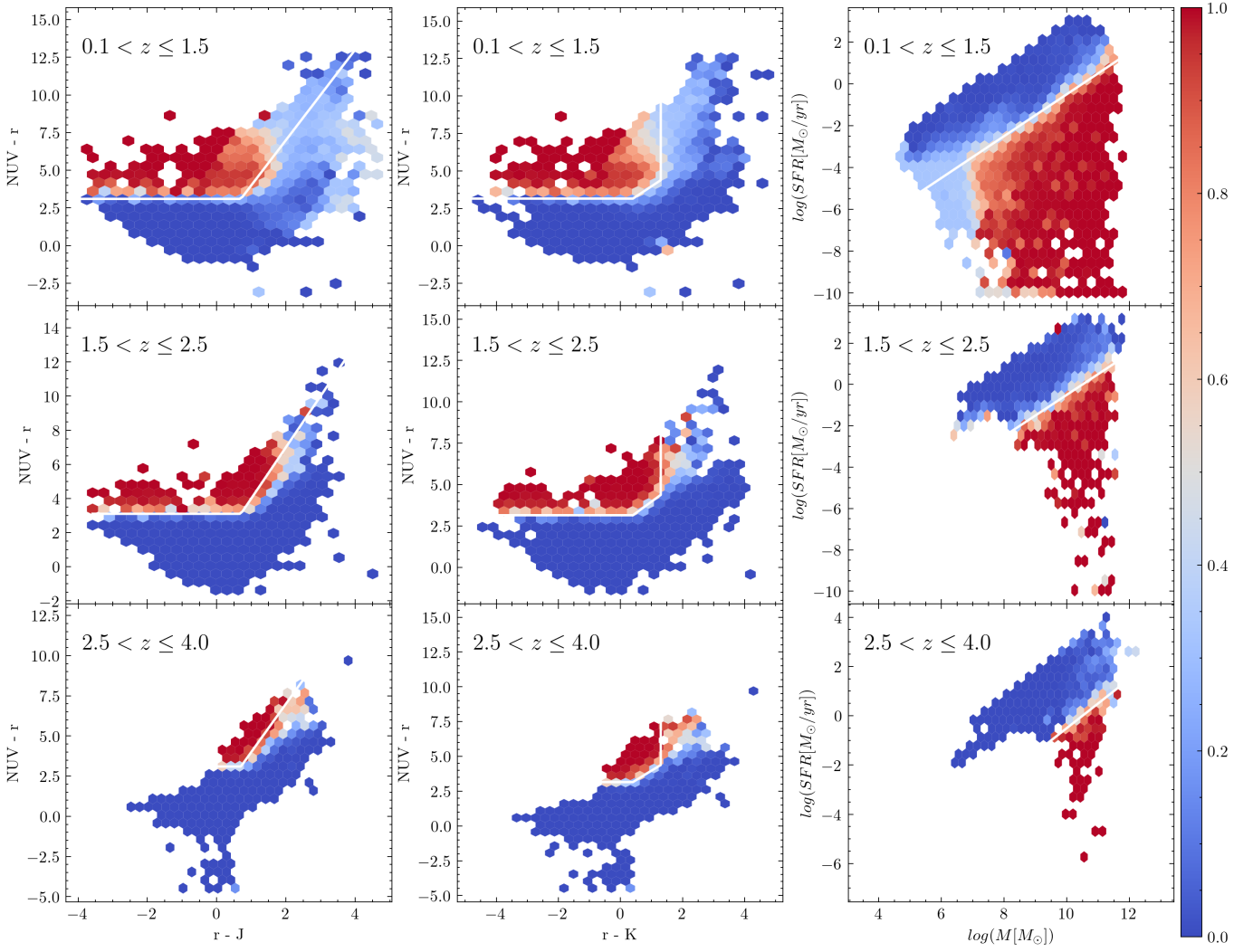


**Fig. 3.** Results of our probabilistic classification of COSMOS-Web galaxies with XGB with imputation, as in the NUVrJ (left column), NUVrK (middle column), and SFR– $M$  (right column) planes. Each hexagon is color-coded by the mean quiescent probability (scale bar on the right), with rows corresponding to different redshift bins. As expected from our training, the method consistently reproduces classical cuts (white lines), while also providing additional insight near the classification boundaries. Classification is ambiguous for some low-mass galaxies at low redshift (light blue region in the top panels).

tified, analogous to completeness. The F1-score combines both precision and recall via their harmonic mean (i.e.  $2PR/P + R$ ). These three quantities range between 0 and 1.

The performances evaluated against the testing set are summarized in Table 1, in terms of the metrics just introduced, both for the minority (quiescent galaxies, red) and for the majority class (star-forming galaxies, blue). The different methods yield comparable results for the classification of star-forming galaxies, whereas for the identification of quiescent galaxies, the XGB algorithm tends to perform better overall. Interestingly, applying SMOTE to help LDA with class unbalance increases recall for the minority class but significantly reduces precision. This may be due to an overlap between the two class distributions, which is expected to increase false positives when synthetic data are injected (e.g. Chawla et al. 2011; Lu et al. 2024).

However, in this application, we are not only concerned with the quality of the binary classification of our target sample, but particularly with the accuracy of the probability assigned to each object for belonging to a class, since this probability is used to estimate quiescent fractions and identify the red sequence. Therefore, besides recall, precision, and F1-score, we analyzed

how well the probability is calibrated. Figure 2 shows the calibration curve, that is, the fraction of positives (star-forming galaxies) versus the mean predicted probability for that class, for the four methods. An example of a model performing well in terms of F1-score but returning a biased calibration curve is the model based on data augmentation for the balancing of classes. Trying to fix unbalanced class data like star-forming and quiescent galaxies possibly results in an injection of false positives (quiescent galaxies classified as star-forming), which pushes the calibration curve above the 1-to-1 relation (see the green lines in Fig. 2). Another behavior displayed by the calibration curves is the sensitivity of LDA to the number of features selected. In simple linear models, a small number of strong features can yield a better calibration than a more complex model based on more galaxy properties.

By implementing the imputation of the missing values instead of complete discard, we observed a slight decrease in the performance for minority class recall, but a better-calibrated probability. For this application, given the importance of a well-calibrated probability and the stability of the algorithm with respect to the number of features used, we decided to opt for an

**Table 1.** Performance of the classification methods in terms of precision, recall, and F1-score. The upper block refers to the training with all available rest-frame magnitude bands, the bottom block to the one using only the four with the highest decision impact.

Method	Precision (red/blue)	Recall (red/blue)	F1-score (red/blue)
<b>NUV,<i>u</i>, <i>r</i>, <i>i</i>, <i>z</i>, <i>Y</i>, <i>J</i>, <i>H</i>, <i>K</i></b>			
LDA	0.94/0.99	0.84/1.00	0.89/0.99
LDA + SMOTE	0.69/1.00	1.00/0.97	0.81/0.98
XGB	0.96/1.00	0.95/1.00	0.95/1.00
XGB with -99.9	0.96/1.00	0.93/1.00	0.94/1.00
<b>NUV,<i>r</i>, <i>J</i>, <i>K</i></b>			
LDA	0.90/0.99	0.90/0.99	0.90/0.99
LDA + SMOTE	0.66/1.00	1.00/0.96	0.80/0.98
XGB	0.96/1.00	0.95/1.00	0.95/1.00
XGB with -99.9	0.95/0.99	0.91/1.00	0.93/1.00

**Notes.** Testing set sample size and red/blue ratio: 94236 galaxies with 7.1% red/blue ratio; 98659 with 7.2% red/blue ratio, when missing values are imputed.

XGB-based classification with the imputation of a constant value for missing data. In Fig. 2, this configuration is represented by the blue dashed line, which is the most stable and closest to the 1-to-1 relation.

The results of our probabilistic classification, applied to the COSMOS2025 dataset used for the COSMOS-Web group search, are shown in Fig. 3: each hexagon is color-coded according to the mean probability to be quiescent (bar on the right) inside that hexagonal bin; each column shows a different diagram used in classical methods, while rows refer to different redshift intervals. As expected from the labeling of our training set, our method is consistently mapping classical empirical cuts (displayed as white lines), while providing additional insight, particularly in regions near the classification boundaries. The algorithm struggles in the classification of galaxies with masses below  $10^7 M_\odot$  in the first redshift bin, populating the light blue region in the top panels. These galaxies mostly have  $z < 0.2$ , and are expected to have a small impact on our analysis, as we are particularly interested in evolution at earlier cosmic times.

In a recent parallel work, Asadi et al. (2025) classified Farmer COSMOS2020 galaxies (Weaver et al. 2022), using a gradient boosted tree algorithm trained on a mock galaxy catalog based on semi-analytical models and using 28 colors. Since the trained model is publicly available, we tested it on the COSMOS-Web data. The results are consistent with what they observe for COSMOS2020: notably, a higher fraction of quiescent galaxies is returned by their model at all redshifts, with respect to classical methods, our classification is based on.

#### 4. Quiescent galaxy fractions

We studied the fraction of quiescent (red) galaxies in groups and its dependencies on group richness and redshift. The quiescent fractions are computed with three different methods: pure membership, secondary association subtraction, and cylinder background subtraction. In all three cases, we analyzed all

galaxies up to 4 magnitudes fainter than the luminosity function knee magnitude,  $m_\star$ , in the reference band, the NIRCам F150W band, which was estimated by evolving a massive elliptical galaxy (see Toni et al. 2025, for details) with evolutionary synthesis models (Kotulla et al. 2009). Given the limiting depth of the galaxy catalog, this choice yields uniform completeness until at least  $z \sim 2.5$ . The quiescent fraction may be slightly overestimated at higher redshifts due to faint star-forming galaxies that are fainter than the catalog limit. In this Section, we will briefly introduce the three approaches to compute the quiescent fraction and present the results for this group sample.

##### 4.1. Pure membership and secondary association subtraction

Our sample includes the probability for each galaxy to belong to a given group, as provided by the AMICO algorithm. Then, we have the probability for each galaxy to be quiescent as we estimated in Sect. 3. The simplest way to compute quiescent fractions is by summing the probabilities to be quiescent, conditional on the probability of belonging to a group, and dividing it by the total, regardless of the class attributed in Sect. 3. Given that  $P_{i,j}$  is the AMICO probability of the  $i$ -th galaxy of belonging to the  $j$ -th group (see Maturi et al. 2019, for details) and that  $P_{red,i}$  and  $P_{blue,i}$  are the (complementary) probabilities of the galaxy to be quiescent or star-forming, respectively, the quiescent fraction of the  $j$ -th group,  $f_{q,j}$ , can be estimated as:

$$f_{q,j} = \frac{\sum P_{red,i} P_{i,j}}{\sum P_{red,i} P_{i,j} + \sum P_{blue,i} P_{i,j}} = \frac{\sum P_{red,i} P_{i,j}}{\sum P_{i,j}}. \quad (1)$$

This computation relies on AMICO membership probabilities, which are model-dependent, computed during the detection process and based on the chosen model of that specific group search, that is built on an NFW profile (Navarro et al. 1997) and a Schechter luminosity function (Schechter 1976), for typical low-mass clusters or large groups (Toni et al. 2024, 2025). The AMICO association probability assignment also takes into account the possibility for a galaxy to be associated with multiple group detections. Thus, we introduced a small correction in the computation, which consists of considering only the main (highest probability) association for each galaxy and subtracting from it the probabilities to be associated with other detections (secondary associations). The probability  $P_{i,j}$  in Eq. 1 is therefore substituted by

$$P_{i,j-new} = P_{i,j-main} - \sum_{N_{assoc}-1} P_{i,j-secondary} \quad (2)$$

However, this correction resulted to be minimal, and the results with and without correction, statistically compatible.

The results are reported in Fig. 4, where we show the weighted quiescent fraction, that is, the quiescent fraction expressed by Eq. 1, weighted by the purity of the sample in the corresponding redshift and richness bin, as estimated against realistic mocks produced with SinFoniA (Maturi et al. 2019) and presented in Toni et al. (2025). The population of quiescent galaxies seems to start building up consistently shortly before  $z = 2$ , starting from the richest systems. The slight increase in quiescent fraction observed at  $z \gtrsim 3$ , albeit minimal, is the expected effect of the  $m_\star + 4$  cut reaching the magnitude limit of the galaxy sample ( $m_{F150W} = 27.3$ ). For this analysis and for the following ones, redshift bin sizes are chosen to homogenize number counts when possible, and error bars are estimated via bootstrapping with 1000 realizations.



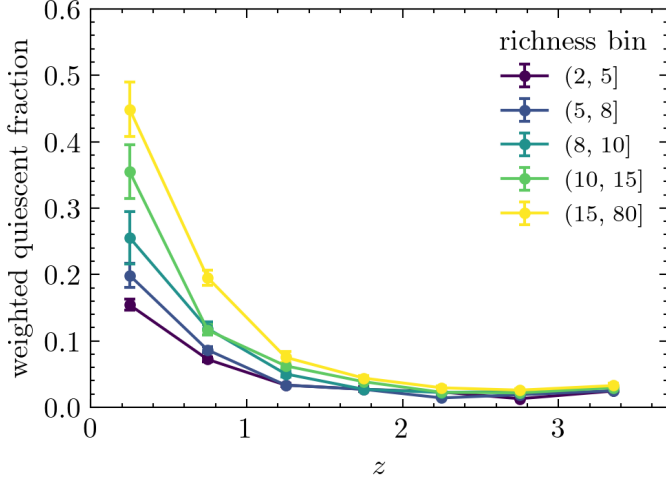


**Fig. 4.** Purity-weighted quiescent fraction vs. redshift in different richness ( $\lambda_*$ ) bins, as in the legend.

#### 4.2. Cylinder background subtraction

The AMICO algorithm produces model-dependent membership probabilities for the group member galaxies. In some cases, when quantities used to model the distribution of galaxies in the template are studied, this might lead to biased considerations due to the underlying model chosen for the detection. This is the case for radial profiles and luminosity functions (see e.g. [Puddu et al. 2021](#)). In [Toni et al. \(2025\)](#), we proposed a new method based on a cylinder-based background subtraction technique to retrieve model-independent results for individual and stacked analyses. For the study of the quiescent fraction, we tested the cylinder method, performing background subtraction and estimating the quiescent fraction in a model-independent way. We proceeded as follows:

1. we defined cylindrical volumes around each group, with radius 0.5 Mpc/h and depth  $\pm 0.01(1+z_g)$  from the group center, where  $z_g$  is the group redshift. We call these 'group regions';
2. we estimated effective unmasked areas on the entire field, using the same mask adopted in the detection process, for consistency, in each redshift slice (using the AMICO redshift resolution,  $\Delta z = 0.01$ ), inside and outside the cylinders, namely for 'group region' and 'field regions', respectively;
3. we estimated quiescent and star-forming galaxy counts as the sum of the probability to be quiescent ( $P_{\text{red}}$ ) or star-forming ( $P_{\text{blue}}$ ), weighted by the value of the galaxy redshift probability distribution at the group redshift. Thus, the red and blue counts are expressed by

$$N_{\text{red}} = \sum_i P_{\text{red},i} p_i(z_j), \text{ and } N_{\text{blue}} = \sum_i P_{\text{blue},i} p_i(z_j), \quad (3)$$

where the  $p_i(z_j)$  is the redshift probability of the  $i$ -th galaxy at the redshift of the host group detection ( $z_j$ );

4. we did this computation for galaxies in both group and field regions and normalized counts by the volumes ( $V_{(1)}$  and  $V_{(0)}$ , respectively), in the redshift slices the cylinder crosses;
5. the final density within groups is the density in the group region minus the density in the field region. Given that the subscripts (1) and (0) refer to galaxies and volumes in the group and field regions, respectively, the final density of quiescent (red) galaxies (equivalent for the star-forming, or blue) in the

$j$ -th group is given by

$$\rho_{\text{red},j} = \sum_{(1)} P_{\text{red},i} p_i(z_j) V_{(1)}^{-1} - \sum_{(0)} P_{\text{red},i} p_i(z_j) V_{(0)}^{-1}; \quad (4)$$

6. finally, the quiescent galaxy fraction is defined as the background-subtracted density of quiescent galaxies over the total density. Galaxies and respective volumes located in the cylinder redshift slices, outside the cylinder volume, and along the line of sight of it, are rejected and not included in the calculation to avoid contamination. Thus, the final expression for the cylinder quiescent galaxy fraction,  $f'_{\text{q},j}$ , is given by

$$f'_{\text{q},j} = \frac{\rho_{\text{red},j}}{\rho_{\text{red},j} + \rho_{\text{blue},j}} \quad (5)$$

$$= \frac{\rho_{\text{red},j}}{\sum_{(1)} p_i(z_j) V_{(1)}^{-1} - \sum_{(0)} p_i(z_j) V_{(0)}^{-1}}. \quad (6)$$

In this computation, as well as for the one using the membership probability, we weighted the quiescent fraction obtained as just described by the value of the purity in the corresponding bins of redshift and richness. Results for cylinder-subtracted quiescent fractions are computed only for groups with  $\lambda_* > 10$  (90%-pure subsample) to reduce the noise and are shown in Fig. 5 for three different bins of richness. For comparison, we report in gray the results for the two highest richness bins from Fig. 4. Apart from having larger uncertainties due also to lower statistics and to the scatter given by the background, the trend with redshift of the cylinder-based fractions is in line with a rapid build-up of the quiescent population starting at  $z \sim 2$ , and  $z \sim 2.5$  for the richest groups, as seen when using pure memberships. However, when present, the quiescent population seems to be more dominant in rich groups when estimated through the cylinder-based method, which may be interpreted as a consequence of the field galaxy contamination removal, but also as an effect of the fixed radius sampling, which might be restricting the computation to the central areas only in the richest groups. The discrepancy is indeed less prominent in the low richness bins. Despite the pure membership being model-dependent, it yields more robust results from a statistical point of view<sup>1</sup>.

#### 4.3. X-ray luminosity of groups and environmental effects

In this Section, we consider the AMICO-COSMOS cluster sample ([Toni et al. 2024](#)) comprising 622 candidate groups with X-ray flux above the significance level. Among these, 222 detections have a robust estimate of X-ray properties that was used to estimate group mass and to calibrate mass-proxy scaling relation in [Toni et al. \(2024\)](#). In this sample, around half of the detections have no significant X-ray emission, and this is fairly independent of  $S/N$  or redshift cuts. We leverage the availability of X-ray flux and X-ray flux significance (i.e.  $\sigma_X$ ) in this sample to study the quiescent fraction and its evolution for the population of X-ray bright groups and those for which a significant X-ray emission was not detected. We calculated the quiescent

<sup>1</sup> It should be noted that, although AMICO does not explicitly use color selections like RS-based detection algorithms, biases may still arise from the intrinsic properties of the data. In particular, quiescent galaxies tend to be massive and systematically brighter than star-forming ones. Even after removing model (and therefore magnitude) dependence via the cylinder method, the analysis may remain affected by the generally higher photo- $z$  accuracy of quiescent galaxies compared to star-forming ones.

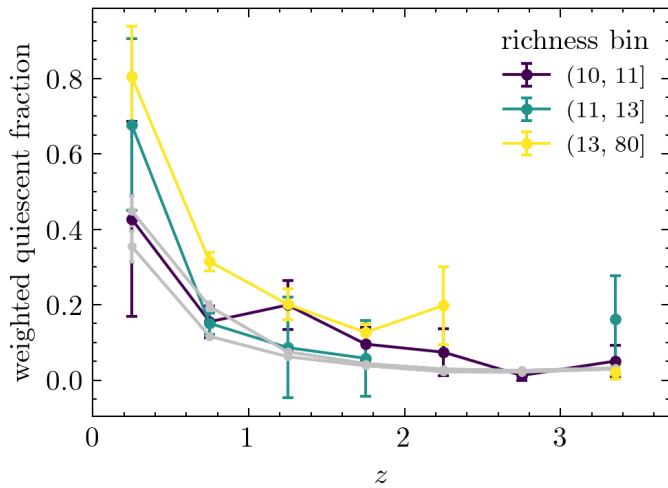


**Fig. 5.** Purity-weighted quiescent fraction as estimated with the cylinder background subtraction, as a function of redshift for groups with  $\lambda_* > 10$ . Different colors show different richness bins, as in the legend. The gray trend lines refer to the two richest bins obtained with the pure membership method (Fig. 4).

fraction with the pure membership method, in order not to limit the statistics of the sample, dividing it into the population of robust X-ray emitters ( $\sigma_X > 1$  and good quality flag from Toni et al. 2024; 164 groups) and the population with X-ray flux under the significance limit ( $\sigma_X \leq 1$ ; 359 groups). The difference between quiescent fraction for the two populations is shown in Fig. 6 as a function of redshift (top panel) and AMICO signal-to-noise ratio,  $S/N_{nocl}$  (bottom panel) for two different richness bins (blue and orange lines). The result is that groups with clear X-ray emission tend to have a quiescent fraction consistently higher than or at most equal to that of groups without significant X-ray emission. In particular, rich groups detected with high  $S/N$  and groups at  $z \leq 0.5$  seem to have significantly more dominant population of quiescent galaxies when they are bright in the X-rays.

In a recent study, Popesso et al. (2024) have compared the GAMA vs eROSITA samples analyzing the properties of X-ray-undetected clusters and groups. Among the considered properties, they have studied the position of the clusters with respect to the large-scale structure (LSS), finding that  $\sim 90\%$  of low-emission clusters and groups, often undetected in the X-rays, are located in filaments (and sheets) rather than in the nodes of the cosmic web. Interestingly, this might be correlating with the properties of the hosted galaxy population, like the pre-accretion processing and therefore the star-formation activity. Groups residing in nodes are more likely to accrete galaxies pre-processed in filaments and, therefore, are more quenched on average. On the other hand, groups hosted by filaments accrete galaxies from the field that are therefore less processed. To check whether this is the case for our sample as well, we compared the position of our groups with that of galaxies that have been found to be located in filaments or in clusters based on local density in LSS maps. For this, we used data from the COSMOS LSS study by Darvish et al. (2014), which covers the redshift interval  $0.1 \leq z \leq 1.4$  and the more recent data based on the COSMOS2020 galaxy catalog, which extends from  $z = 0.5$  to beyond the higher end of our group sample (Taamoli et al, in prep.).

The results of this test are shown in Fig. 7 for the COSMOS2020-based LSS; results for the LSS map by Darvish et al. (2014) show very similar trends. In Fig. 7, the horizontal axis represents the filament signal, defined as the ratio of the

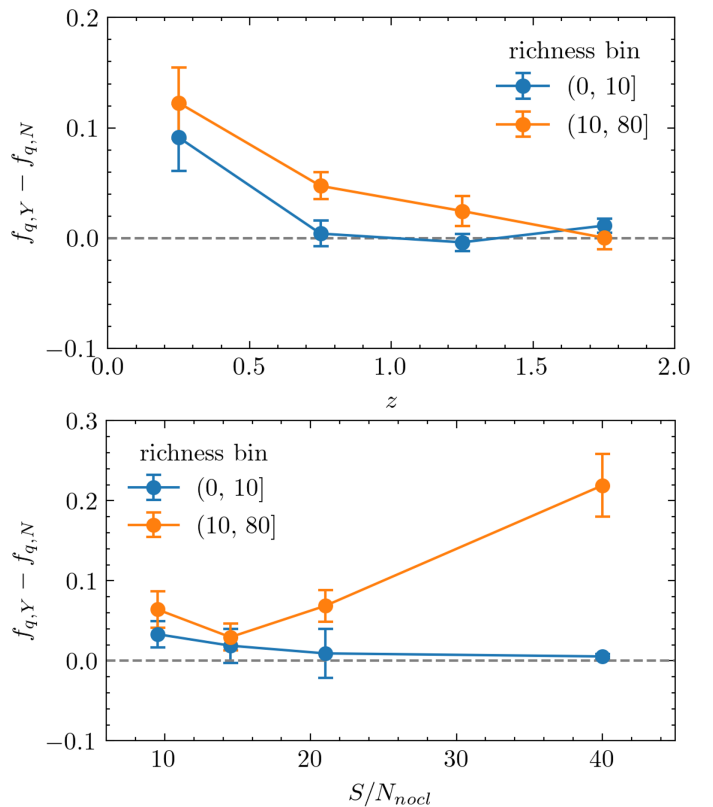


**Fig. 6.** Quiescent fraction difference between X-ray bright (Y) and X-ray faint (N) groups as a function of redshift (top panel) and AMICO  $S/N_{nocl}$  (bottom panel), in two bins of richness as in the legend.

number of filament galaxies in a cylinder centered on the group to the number of filament + cluster galaxies, while the vertical axis indicates the probability density distribution smoothed and normalized using Kernel Density Estimation (KDE). Groups without significant X-ray emission (pink curve) have around 2 times higher density in filaments (filament signal  $> 0.8$ ) with respect to X-ray bright ones (green curve). The latter are instead more likely to be found in denser environments in correspondence or close to cosmic-web nodes (filament signal  $< 0.2$ ).

Interesting insights can be gained from the investigation of group properties through a comparison between optically selected and X-ray selected clusters and groups. A comprehensive analysis of this aspect, for what concerns the AMICO-COSMOS groups and that incorporates the X-ray characterization of the new COSMOS-Web group catalog, will be presented in a forthcoming dedicated paper.

## 5. Red sequence

We now turn our attention to how the red sequence in our group sample evolves over a wide range of redshifts, from  $z = 0$  to  $z = 3.7$ . To study this, we need to identify the red sequence and characterize it through the main parameters of the RS ridgeline.

### 5.1. Observed red sequence with rest-frame matching

The first step to robustly detect the observed red sequence is to identify the appropriate combination of colors and magnitude that, at a given redshift, allow a clean identification of the sequence in the CMD. This can be done following the matched rest-frame photometry method (Blakeslee et al. 2006; Stott et al.



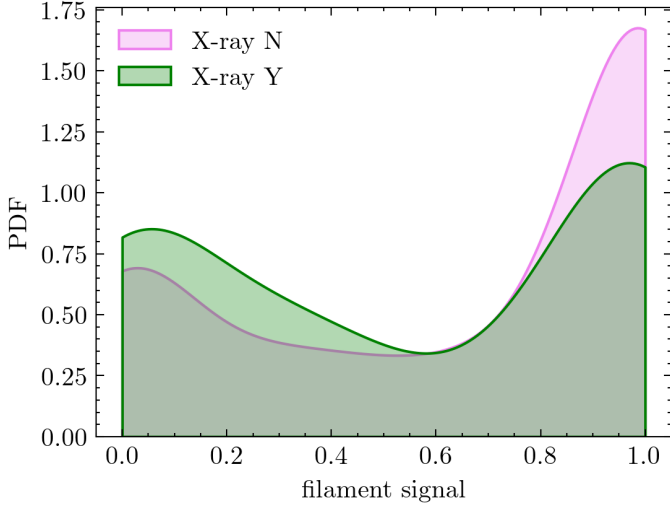


**Fig. 7.** Filament signal (ratio of number of filament galaxies to number of filament and cluster galaxies) probability density function for X-ray bright (Y) and X-ray faint (N) groups, using the LSS data and galaxy classification by Taamoli et al. in prep. Consistent results are obtained using the LSS information provided by Darvish et al. (2014)

2009), namely by choosing two magnitude bands that bracket a characterizing spectral feature, like the 4000 Å break, and the reddest of the two as the reference magnitude for the CMD. This reduces the impact of the  $k$ -correction and the redshift dependence of the colors, straddling a feature that strongly traces different stellar populations in RS and non-RS galaxies.

The COSMOS-Web galaxy catalog features a comprehensive set of magnitude bands spanning from optical to mid-infrared wavelengths. This coverage is uniform and continuous thanks to the complementarity of the JWST NIRCcam filters and the UltraVISTA filters, making this the perfect opportunity to study observed red sequence evolution over a wide interval of redshifts, using the matched rest-frame photometry technique. This can be seen in Fig. 8, which shows the observed wavelength of the rest-frame 4000 Å break (black solid line) at different redshifts over the studied interval, and which filters are sampling and bracketing it (vertical dashed lines indicate when the break exists and enters adjacent bands). As clearly visible, the filter coverage of this spectral feature is continuous until at least  $z \sim 3.5$ , namely virtually covering the full COSMOS-Web group sample. Our selection of the 4000Å-bracketing band pairs and the relative intervals are shown in Table 2. Once the red sequence is sampled in consistent observed colors, the ridgeline can be identified as the best-fitting line representing the locus of the quiescent member galaxies in the CMD.

**Table 2.** Red-sequence selection method: observed color and magnitude choices by redshift interval.

Redshift Range	Color	Magnitude
$0.01 < z < 0.38$	$g - r$	$r$
$0.38 < z < 0.70$	$r - i$	$i$
$0.70 < z < 1.10$	$i - z$	$z$
$1.10 < z < 1.40$	$z - Y$	$Y$
$1.40 < z < 1.70$	$Y - J$	$J$
$1.70 < z < 2.35$	F115W – F150W	F150W
$2.35 < z < 3.25$	F150W – $H$	$H$
$3.25 < z < 3.70$	$H - K_s$	$K_s$

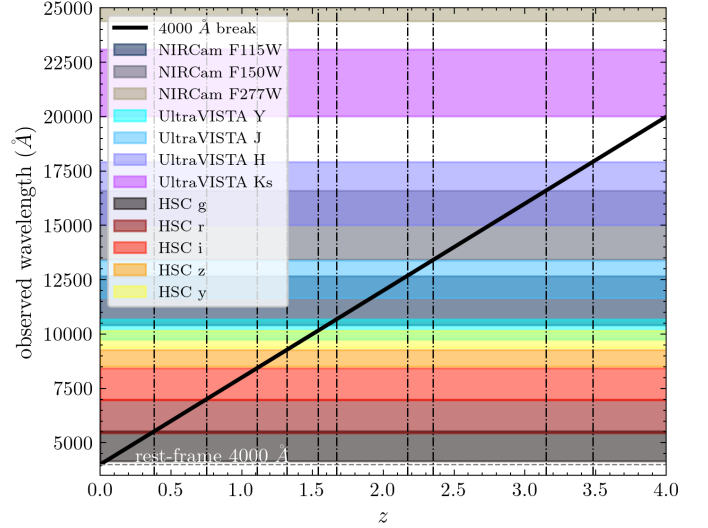


**Fig. 8.** The sampling in the COSMOS-Web filters of the observed 4000 Å, the spectral feature used for RS detection (black solid line). Different colors indicate different bands, as in the legend, while vertical lines are the exit/enter point of the break in adjacent bands. Pairs of bands bracketing the break are reported in Table 2. The coverage is contiguous up to  $z \sim 3.5$ .

As in Sect. 4, we performed this RS analysis over 4 magnitudes from the  $m_*$  in the F150W band, which, given the depth of the galaxy catalog, guarantees redshift-dependent completeness until at least  $z \sim 2.5$ , without compromising the statistics. We computed the RS parameters by performing a weighted least squares (WLS) fitting analysis of the group CMDs on all galaxies attributed to a group with a probability larger than the minimum threshold imposed by AMICO, that is, 0.005. In a similar way to what we have done for the red fraction in Sect. 4.1, we weighted each galaxy with the probability of being quiescent, conditional on the probability of being a group member. This represents the first guess for the position of the red sequence, which is nevertheless still potentially contaminated by central and/or bright star-forming galaxies that might draw the ridgeline guess towards bluer colors. To refine the position guess, we performed an iterative cleaning of outliers by fitting with a  $3\sigma$  clipping. Once convergence is reached (over maximum 5 iterations), the following RS best-fit parameters are stored for each group detection: the scatter computed on final retained galaxies, the average color, which is the color of the RS ridgeline computed at  $m_*$  and the number of RS galaxies, which we defined as the number of quiescent member galaxies ( $P_{red} > 50\%$  and  $P > 50\%$ ) lying within a typical  $\pm 0.3$  scatter (e.g. De Lucia et al. 2007; Martinet et al. 2015) from the best-fit line.

Besides the number of RS galaxies, we also computed  $\lambda_{RS}$ , which is the sum of the membership probability of RS galaxies, in analogy to AMICO apparent richness,  $\lambda$ . Figure 9 shows the fraction of  $\lambda_{RS}$  to the  $\lambda$  (sum of all membership probabilities of galaxies used for the initial guess) as a function of redshift, for the sample of groups with an RS identified with  $\lambda_{RS} > 2$ . This is an arbitrary limit that roughly corresponds to having at least 3 quiescent galaxies on the RS ridgeline. The yellow line and points indicate the average trend of the RS fraction with redshift. The size of the red points is proportional to the  $S/N$  of the group detection, which is used as a weight for the average. The grey trend line is reported from the quiescent fraction analysis for the central richness bin (see Fig. 4), while the blue trend line shows the same as done with the apparent magnitude but using rest-

frame  $J$  and  $Ks$ , which we describe in Sect. 5.2. In the bottom plot, we show instead the fraction of groups with an identified RS with  $\lambda_{RS} > 2$  over the total number of detections per redshift bin, for  $S/N$ -cut at 6, 7, and 10 (i.e., purity level of 77%, 80%, and 90%). The trend follows that of the quiescent fraction and RS fraction. The peak at  $z \sim 0.7 - 0.8$  may be due to the presence of the COSMOS Wall (Iovino et al. 2016), which hosts more mature systems with established red sequences. The total number of groups with an identified RS with  $\lambda_{RS} > 2$  is 214.

The highest-redshift RS detected in this study is located at  $z = 3.4$  and it contains 3 quiescent member galaxies with very similar colors within around 250 kpc/h from each other. This high- $z$  object is among the new protocluster cores not known in the literature before, we reported in Toni et al. (2025), detected independently in a parallel work presented by Hung et al. (2025). The protocluster core contains 5 galaxies with spectroscopic redshift, according to our spectroscopic counterpart assignment in the COSMOS spec- $z$  compilation (Khostovan et al. 2025). The spectroscopic redshifts are compatible with that assigned by AMICO, solely based on photometry, which confirms the presence of an overdensity of galaxies at this location. However, none of the quiescent galaxies of the RS we found have a public spec- $z$  available. If confirmed, this would represent one of the highest-redshift examples of early red sequence detected to date (see the  $z \sim 4$  protocluster reported by Tanaka et al. 2024, and the overdensity discovered at  $z = 3.44$  by Jin et al. 2024). The CMD of this  $z = 3.4$  detection (ID CW117) is shown in Fig. 10, where we plot AMICO member galaxies with size proportional to their membership probability and their color referring to the probability of being quiescent and field galaxies as grey points. In the plot, we also report the main parameters of the RS ridgeline and the RS richness ( $\lambda_{RS}$ ), while the RS galaxies are marked by black circles around the points. The orange dashed line indicates the expected color of a population passively evolving since  $z = 5$ , which is our reference model. This represents the color of a typical  $m_*$ -galaxy, according to the same configuration chosen for the AMICO model used for the group search. The model was computed with the evolutionary synthesis model generator GALEV (Kotulla et al. 2009), relying on a Kroupa initial mass function (Kroupa 2002) and adopting a chemically consistent approach (see Kotulla et al. 2009, for further details) for a massive elliptical formed at  $z_f = 8$  with a more recent medium-intensity (0.2) star-formation burst at  $z = 5$ . This approach is similar to the one already used by Castignani et al. (2022, 2023). In the bottom left of the panel, we report the sky distribution of the galaxies in the central region of this high- $z$  overdensity, with the same notation as in the CMD plot.

## 5.2. Results and comparison with rest-frame red sequence

We performed RS fitting with the same procedure described above ( $3\sigma$ -clipped fit on WLS initial guess) based on the LePhare rest-frame magnitudes in the UltraVISTA- $J$  and  $-Ks$  bands available in the COSMOS2025 release. We confirmed all RS detected with the observed magnitudes, mostly with compatible parameters. We additionally detected RS (mainly with low richness,  $\lambda_{RS} < 3$ ) for another 11 groups.

The RS parameters as a function of redshift for the RS ridgelines detected in this study are shown in Fig. 11. The top panel shows the average observed color for all the detections in the COSMOS-Web group catalog, compared to the reference model we described above in Sect 5.1 (orange lines). Colors are computed in the associated redshift-dependent bands, as summarized in Table 2, which explains the jumps in average color when the

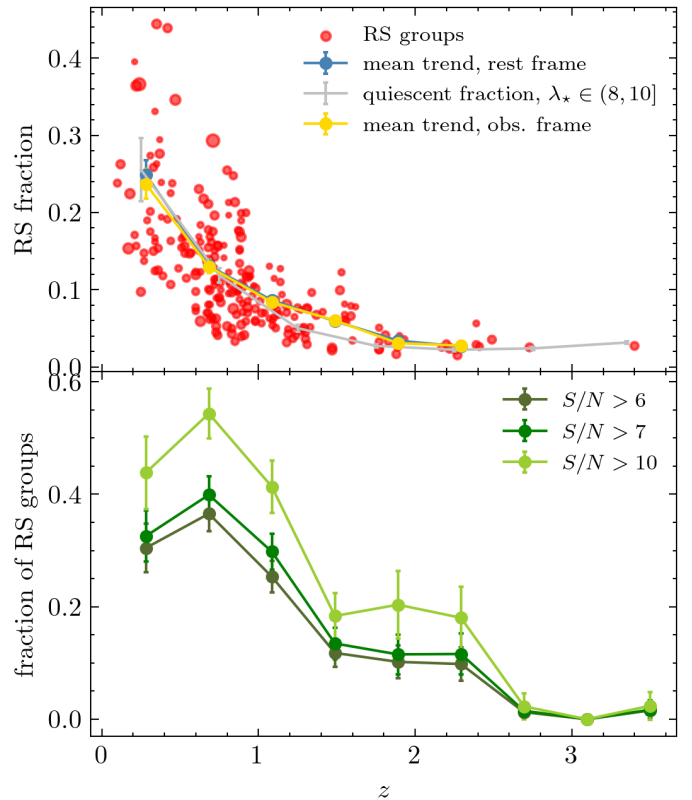


**Fig. 9.** Top panel: fraction of the selected RS galaxies over the total ( $\lambda_{RS}/\lambda$ ) in each group, as a function of redshift for the sample with identified red sequence. The yellow and blue lines indicate the mean fraction in each  $z$ -bin weighted by the group  $S/N$  (size of red points is proportional to the group  $S/N$ ). Bottom panel: the fraction of groups with identified red sequence at different  $S/N$  (or purity) levels, as a function of redshift.

4000 Å switches between adjacent bands. Besides this effect, the trend of the model is consistent with the evolution of the observed colors in our sample until at least  $z \sim 2.4$ . For the last two redshift intervals, the observed color of the ridgeline is not consistent with a prototypical quiescent galaxy, which is expected since at this redshift we do not fit any red sequence for most of the groups, and the ridgeline parameters are tentative and mainly driven by bright star-forming galaxies populating groups and cores at such high redshifts. The location in the plot of the highest- $z$  RS presented above (CW117) is indicated by a yellow star. As already mentioned, the average observed color of this RS is consistent with the model. The second and third panels show the ridgeline slope. In the second plot, we include all groups in the sample (grey points) with the relative total fitted trend (black line) and its  $1\sigma$  error (shaded area). Red points mark groups for which it was possible to identify a red sequence with  $\lambda_{RS} > 2$ . The same sample is shown in the third plot from the top, where we compare the slope computed with observed rest-frame matched colors (red points and orange line and shaded area) with that based on rest-frame  $J$  and  $Ks$  magnitudes (blue points and blue line and shaded area). The two trends are consistent within confidence intervals. The trends suggest a slight decrease (steepening) of the slope with redshift, which, under the assumption of negligible  $k$ -correction effect, may be related to metallicity evolution (e.g. Stott et al. 2009). However, the steepening of the RS over the studied redshift range is very mild, and there is no clear evidence of a significant steepening, in agree-

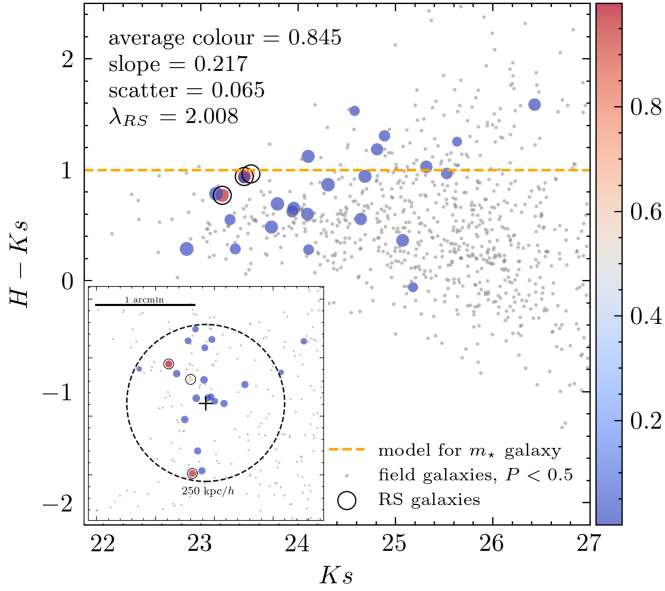


**Fig. 10.** Observed-frame CMD of an overdensity of galaxies at  $z = 3.4$  (CW117) with 3 quiescent galaxies (red points with black contours) with colors consistent with RS evolutionary synthesis models for a typical  $m_*$  elliptical (orange line). This is the highest RS we detected.

ment with, for instance, Mei et al. (2009); Cerulo et al. (2016). A typically adopted slope for the RS (Durret et al. 2011) is shown as a dashed dark red line for comparison. Once again, the location of CW117 is indicated by a yellow star, with red contours for observed colors and blue contours for the rest frame. The same is shown in the fourth and last panel from the top, but for the RS scatter. As for the slope, the results are consistent with no evolution over the studied redshift range, with a mild increase of scatter for the observed frame. The RS scatter is found to be below 0.10 mag for most of the detections, especially when measured in the rest frame. This is consistent with analytical models and studies performed on observed cluster properties (e.g. Hao et al. 2009; Menci et al. 2008; Cerulo et al. 2016).

## 6. Conclusions

We conducted a study of the evolution in redshift and the dependence on group richness of the quiescent galaxy fraction and of the red-sequence parameters for COSMOS groups detected with the AMICO algorithm, across around 12 Gyrs of cosmic history, from  $z = 0$  to  $z = 3.7$ . We have used multiple complementary methods to estimate the quiescent fraction and detect the red sequence, finding consistent results across different approaches. In total, we identified 225 red-sequence ridgelines using rest-frame colors, with 214 also consistently characterized using rest-frame-matched observed colors. The main results of our study are as follows:

- Machine learning classifiers (both linear and non-linear) provide a powerful framework for leveraging photometric multi-band survey data to robustly distinguish between quiescent and star-forming galaxies. In particular, gradient boosting decision trees, such as XGB, offer efficient handling of missing data and class imbalance, while delivering accurate probabilistic classifications. In our application, this approach achieved an F1-score exceeding 93%, even in the case of limited availability of rest-frame magnitudes.

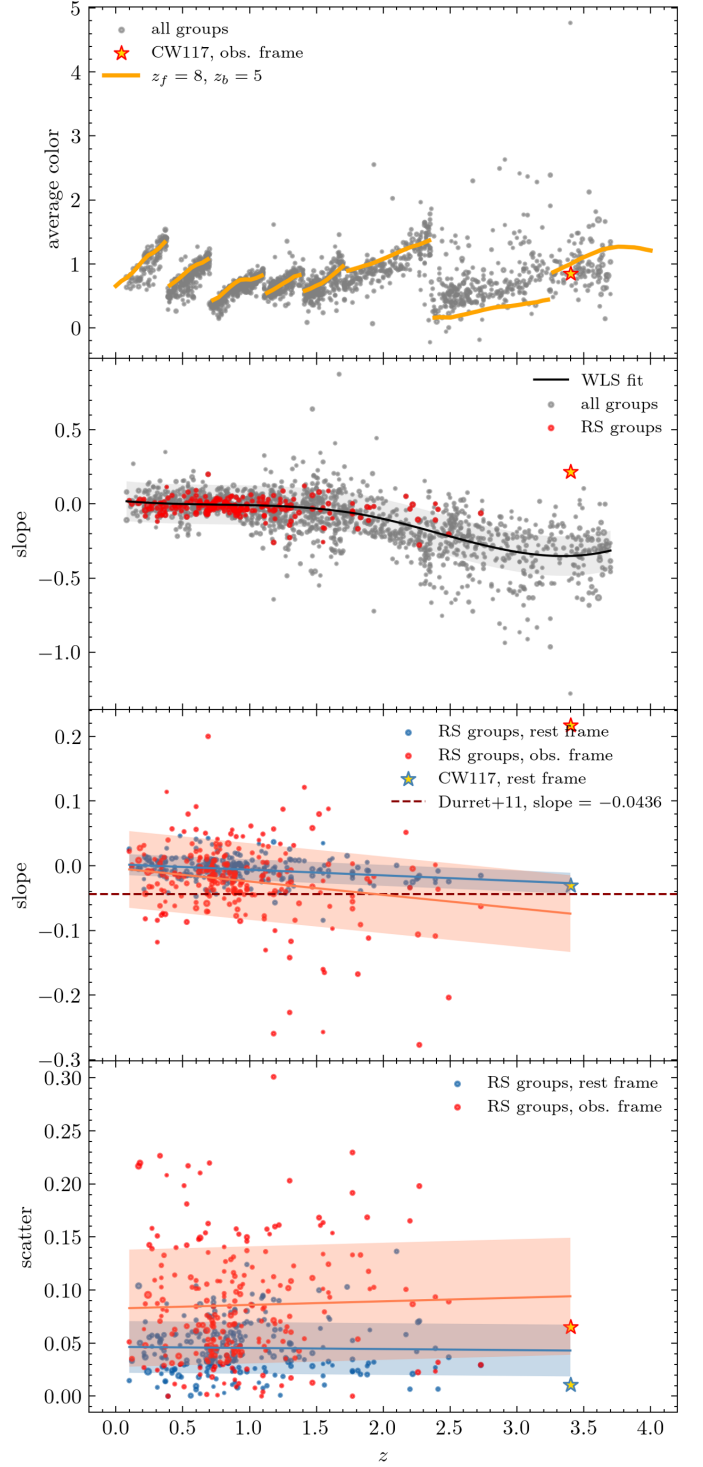


**Fig. 11.** The main red-sequence parameters vs redshift, from top to bottom: the average observed color compared to our reference model (orange lines), the slope, a zoom on the slope of RS-groups only, the scatter for RS-groups only. Grey represents the full sample, red the RS-only groups in the observed frame, and blue in rest frame.

- The AMICO algorithm identifies galaxy groups without relying explicitly on color information. As a result, the AMICO catalogs enable a robust analysis of member galaxy properties, such as colors and luminosities, in both model-dependent and model-independent ways. Our results on the



build-up of the quiescent galaxy population are found to be consistent across these methods.

- By analyzing X-ray characterized AMICO detection, we found an indication that X-ray faint groups show, on average, lower quiescent fractions than X-ray bright ones. This might be connected to their location in the cosmic web, as X-ray faint groups are more likely to be found in filaments, where the environmental pre-processing of galaxies is lower compared to cosmic nodes, as well as the local density.
- We detected and characterized 225 RS ridgelines in COSMOS-Web groups, providing an extensive redshift coverage. We report the discovery of a rare compact ( $\sim 250$  kpc/h scale) overdensity of quiescent galaxies at  $z = 3.4$ , which, if confirmed, may represent one of the most distant early red sequences detected to date, not known in the literature before our recent group search in COSMOS-Web.
- We found that the observed average colors of the red-sequence ridgelines in our sample are consistent with those predicted by a passively evolving elliptical galaxy model. Regarding the slope and scatter of the red sequence, we observed no significant evolution with redshift, in agreement with previous findings for more massive galaxy clusters.

This study extends the detection and characterization of the red sequence and quiescent galaxy fractions beyond  $z > 1.5$  and into the regime of galaxy groups. Such an analysis is a natural application of a deep and well-characterized dataset like the COSMOS-Web group catalog. Especially for high- $z$  candidates and RS evolution trends, we stress the necessity of spectroscopic confirmation, which we plan to carry out in a dedicated campaign. In forthcoming work, we will further investigate the correlation between galaxy properties and X-ray emission (i.e., intracluster/-group medium properties) and its connection with the LSS. Additionally, we plan to explore the properties and role of the central brightest galaxies (BGGs), examining how their evolution relates to the environment and the assembly history of their hosts.

*Acknowledgements.* GT thanks David P. Petri for the valuable discussion and useful suggestions about Machine Learning. LM acknowledges the financial contribution from the PRIN-MUR 2022 20227RNL3 grant “The concordance cosmological model: stress-tests with galaxy clusters” supported by Next Generation EU and from the grant ASI n. 2024-10-HH.0 “Attività scientifiche per la missione Euclid – fase E.

## References

- Aihara, H., AlSayyad, Y., Ando, M., et al. 2022, *PASJ*, 74, 247
- Alberts, S., Pope, A., Brodwin, M., et al. 2016, *ApJ*, 825, 72
- Andreon, S. 2006, *MNRAS*, 369, 969
- Andreon, S. & Huertas-Company, M. 2011, *A&A*, 526, A11
- Arnouts, S., Moscardini, L., Vanzella, E., et al. 2002, *MNRAS*, 329, 355
- Asadi, V., Chartab, N., Zonoozi, A. H., & Haghi, H. 2025
- Baldwin, J. A., Phillips, M. M., & Terlevich, R. 1981, *PASP*, 93, 5
- Balogh, M. L., Schade, D., Morris, S. L., et al. 1998, *ApJ*, 504, L75
- Bellagamba, F., Maturi, M., Hamana, T., et al. 2011, *MNRAS*, 413, 1145
- Bellagamba, F., Roncarelli, M., Maturi, M., & Moscardini, L. 2018, *MNRAS*, 473, 5221
- Bertin, E., Schefer, M., Apostolakis, N., et al. 2022, *ascl*:2212.018
- Bisigello, L., Kuchner, U., Conselice, C. J., et al. 2020, *MNRAS*, 494, 2337
- Blakeslee, J. P., Holden, B. P., Franx, M., et al. 2006, *ApJ*, 644, 30
- Brodwin, M., Stanford, S. A., Gonzalez, A. H., et al. 2013, *ApJ*, 779, 138
- Bruzual, G. & Charlot, S. 2003, *MNRAS*, 344, 1000
- Casey, C. M., Kartaltepe, J. S., Drakos, N. E., et al. 2023, *ApJ*, 954, 31
- Castignani, G., Radovich, M., Combes, F., et al. 2022, *A&A*, 667, A52
- Castignani, G., Radovich, M., Combes, F., et al. 2023, *A&A*, 672, A139
- Cerulo, P., Couch, W. J., Lidman, C., et al. 2016, *MNRAS*, 457, 2209
- Chartab, N., Mobasher, B., Darvish, B., et al. 2020, *ApJ*, 890, 7
- Chawla, N. V., Bowyer, K. W., Hall, L. O., & Kegelmeyer, W. P. 2011
- Chen, T. & Guestrin, C. 2016
- Civano, F., Marchesi, S., Comastri, A., et al. 2016, *ApJ*, 819, 62
- Darvish, B., Sobral, D., Mobasher, B., et al. 2014, *ApJ*, 796, 51
- Davidzon, I., Cucciati, O., Bolzonella, M., et al. 2016, *A&A*, 586, A23
- de Graaff, A., Setton, D. J., Brammer, G., et al. 2025, *Nat. Astron.*, 9, 280
- De Lucia, G., Poggianti, B. M., Aragón-Salamanca, A., et al. 2007, *MNRAS*, 374, 809
- De Lucia, G., Weinmann, S., Poggianti, B. M., Aragón-Salamanca, A., & Zaritsky, D. 2012, *MNRAS*, 423, 1277
- Dressler, A. 1980, *ApJ*, 236, 351
- Durret, F., Laganá, T. F., & Haider, M. 2011, *A&A*, 529, A38
- Euclid Collaboration: Adam, R., Vannier, M., et al. 2019, *A&A*, 627, A23
- Euclid Collaboration: Humphrey, A., Bisigello, L., et al. 2023, *A&A*, 671, A99
- Fisher, R. A. 1936, *Annals of Eugenics*, 7, 179
- Franco, M., Casey, C. M., Koekemoer, A. M., et al. 2025
- Friedman, J. H. 2000, *Ann. Stat.*, 29, 5
- Fritz, A., Scodreggio, M., Ilbert, O., et al. 2014, *A&A*, 563, A92
- Gallazzi, A., Bell, E. F., Zibetti, S., Brinchmann, J., & Kelson, D. D. 2014, *ApJ*, 788, 72
- Gladders, M. D. & Yee, H. K. C. 2000, *Astron. J.*, 120, 2148
- Hao, J., Koester, B. P., McKay, T. A., et al. 2009, *ApJ*, 702, 745
- Harish, S., Kartaltepe, J. S., Liu, D., et al. 2025
- Hasinger, G., Cappelluti, N., Brunner, H., et al. 2007, *ApJS*, 172, 29
- Hennig, C., Mohr, J. J., Zenteno, A., et al. 2017, *MNRAS*, 467, 4015
- Hung, D., Lemaux, B. C., Cucciati, O., et al. 2025, *ApJ*, 980, 155
- Ilbert, O., Arnouts, S., Le Floc’h, E., et al. 2015, *A&A*, 579, A2
- Ilbert, O., Arnouts, S., McCracken, H. J., et al. 2006, *A&A*, 457, 841
- Ilbert, O., Capak, P., Salvato, M., et al. 2009, *ApJ*, 690, 1236
- Ilbert, O., McCracken, H. J., Le Fèvre, O., et al. 2013, *A&A*, 556, A55
- Iovino, A., Petropoulou, V., Scodreggio, M., et al. 2016, *A&A*, 592, A78
- Ito, K., Valentino, F., Farcy, M., et al. 2025, *A&A*, 697, A111
- Jin, S., Sillassen, N. B., Magdis, G. E., et al. 2024, *A&A*, 683, L4
- Khostovan, A. A., Kartaltepe, J. S., Salvato, M., et al. 2025, *arXiv:2503.00120*
- Kodama, T. & Arimoto, N. 1997, *A&A*, 320, 41
- Koekemoer, A. M., Aussel, H., Calzetti, D., et al. 2007, *ApJS*, 172, 196
- Kotulla, R., Fritze, U., Weibacher, P., & Anders, P. 2009, *MNRAS*, 396, 462
- Kravtsov, A. V. & Borgani, S. 2012, *Annu. Rev. Astron. Astrophys.*, 50, 353
- Kroupa, P. 2002, *Science*, 295, 82
- Laigle, C., McCracken, H. J., Ilbert, O., et al. 2016, *ApJS*, 224, 24
- Lu, X., Ye, X., & Cheng, Y. 2024
- Lundberg, S. & Lee, S.-I. 2017
- Marinetti, N., Durret, F., Guennou, L., et al. 2015, *A&A*, 575, A116
- Maturi, M., Bellagamba, F., Radovich, M., et al. 2019, *MNRAS*, 485, 498
- McCracken, H. J., Milvang-Jensen, B., Dunlop, J., et al. 2012, *A&A*, 544, A156
- Mei, S., Holden, B. P., Blakeslee, J. P., et al. 2009, *ApJ*, 690, 42
- Menci, N., Rosati, P., Gobat, R., et al. 2008, *ApJ*, 685, 863
- Moneti, A., McCracken, H. J., Hudelot, W., et al. 2023, *VizieR*, 2373, II/373
- Navarro, J. F., Frenk, C. S., & White, S. D. M. 1997, *ApJ*, 490, 493
- Pearson, W. J., Pistis, F., Figueira, M., et al. 2023, *A&A*, 679, A35
- Pedregosa, F., Varoquaux, G., Gramfort, A., et al. 2011, *JMLR*, 12, 2825
- Peng, Y.-j., Lilly, S. J., Kovač, K., et al. 2010, *ApJ*, 721, 193
- Popesso, P., Biviano, A., Bulbul, E., et al. 2024, *MNRAS*, 527, 895
- Puddu, E., Radovich, M., Sereno, M., et al. 2021, *A&A*, 645, A9
- Radovich, M., Tortora, C., Bellagamba, F., et al. 2020, *MNRAS*, 498, 4303
- Rieke, M. J., Kelly, D. M., Misselt, K., et al. 2023, *PASP*, 135, 028001
- Rudnick, G., von der Linden, A., Pelló, R., et al. 2009, *ApJ*, 700, 1559
- Rykoff, E. S., Rozo, E., Busha, M. T., et al. 2014, *ApJ*, 785, 104
- Rykoff, E. S., Rozo, E., Hollowood, D., et al. 2016, *ApJS*, 224, 1
- Salim, S., Boquien, M., & Lee, J. C. 2018, *ApJ*, 859, 11
- Sawicki, M., Arnouts, S., Huang, J., et al. 2019, *MNRAS*, 489, 5202
- Schechter, P. 1976, *Astrophys. J. Vol 203 P 297-306* 1976, 203, 297
- Scoville, N., Aussel, H., Brusa, M., et al. 2007, *ApJS*, 172, 1
- Shimakawa, R., Koyama, Y., Röttgering, H. J. A., et al. 2018, *MNRAS*, 481, 5630
- Shuntov, M., Akins, H. B., Paquereau, L., et al. 2025, *arXiv:2506.03243*
- Smolčić, V., Novak, M., Bondi, M., et al. 2017, *A&A*, 602, A1
- Spitler, L. R., Labbé, I., Glazebrook, K., et al. 2012, *ApJ*, 748, L21
- Stott, J. P., Pimbblet, K. A., Edge, A. C., Smith, G. P., & Wardlow, J. L. 2009, *MNRAS*, 394, 2098
- Strazzullo, V., Daddi, E., Gobat, R., et al. 2016, *ApJ*, 833, L20
- Strazzullo, V., Gobat, R., Daddi, E., et al. 2013, *ApJ*, 772, 118
- Taamoli, S., Nezhad, N., Mobasher, B., et al. 2024
- Tanaka, M., Onodera, M., Shimakawa, R., et al. 2024, *ApJ*, 970, 59
- Taniguchi, Y., Kajisawa, M., Kobayashi, M. A. R., et al. 2015, *PASJ*, 67, 104
- Toni, G., Gozaliasl, G., Maturi, M., et al. 2025, *A&A*, 697, A197
- Toni, G., Maturi, M., Finoguenov, A., Moscardini, L., & Castignani, G. 2024, *A&A*, 687, A56
- Wang, T., Elbaz, D., Daddi, E., et al. 2016, *ApJ*, 828, 56
- Weaver, J. R., Kauffmann, O. B., Ilbert, O., et al. 2022, *ApJS*, 258, 11
- Whitaker, K. E., Labbé, I., van Dokkum, P. G., et al. 2011, *ApJ*, 735, 86
- Wright, R. H., Sabatke, D., & Telfer, R. 2022, 12180, 121803P

Zavala, J. A., Casey, C. M., Scoville, N., et al. 2019, *ApJ*, 887, 183  
 Zheng, Y., Xu, K., Zhao, D., et al. 2025, *ApJ*, 984, 193

- <sup>1</sup> University of Bologna, Department of Physics and Astronomy “Augusto Righi” (DIFA), Via Gobetti 93/2, I-40129 Bologna, Italy
- <sup>2</sup> INAF – Osservatorio di Astrofisica e Scienza dello Spazio, Via Gobetti 93/3, I-40129 Bologna, Italy
- <sup>3</sup> Zentrum für Astronomie, Universität Heidelberg, Philosophenweg 12, D-69120 Heidelberg, Germany
- <sup>4</sup> Institut für Theoretische Physik, Universität Heidelberg, Philosophenweg 16, D-69120 Heidelberg, Germany
- <sup>5</sup> INFN – Sezione di Bologna, Viale Berti Pichat 6/2, I-40127 Bologna, Italy
- <sup>6</sup> Department of Computer Science, Aalto University, P.O. Box 15400, FI-00076 Espoo, Finland
- <sup>7</sup> Department of Physics, University of Helsinki, P.O. Box 64, FI-00014 Helsinki, Finland
- <sup>8</sup> Department of Physics and Astronomy, University of California, Riverside, 900 University Avenue, Riverside, CA 92521, USA
- <sup>9</sup> Department of Astronomy, The University of Texas at Austin, 2515 Speedway Blvd Stop C1400, Austin, TX 78712, USA
- <sup>10</sup> Aix Marseille Univ, CNRS, CNES, LAM, Marseille, France
- <sup>11</sup> Department of Physics, University of California, Santa Barbara, Santa Barbara, CA 93106, USA
- <sup>12</sup> Cosmic Dawn Center (DAWN), Denmark
- <sup>13</sup> Department of Physics and Astronomy, University of Hawaii, Hilo, 200 W Kawili St, Hilo, HI 96720, USA
- <sup>14</sup> Caltech/IPAC, MS 314-6, 1200 E. California Blvd., Pasadena, CA 91125, USA
- <sup>15</sup> Laboratory for Multiwavelength Astrophysics, School of Physics and Astronomy, Rochester Institute of Technology, 84 Lomb Memorial Drive, Rochester, NY 14623, USA
- <sup>16</sup> Université Paris-Saclay, Université Paris Cité, CEA, CNRS, AIM, 91191 Gif-sur-Yvette, France
- <sup>17</sup> DTU Space, Technical University of Denmark, Elektrovej 327, 2800 Kgs. Lyngby, Denmark
- <sup>18</sup> Department of Physics and Astronomy, University of Kentucky, 505 Rose Street, Lexington, KY 40506, USA
- <sup>19</sup> Space Telescope Science Institute, 3700 San Martin Drive, Baltimore, MD 21218, USA
- <sup>20</sup> Institute for Computational Cosmology, Department of Physics, Durham University, South Road, Durham DH1 3LE, United Kingdom
- <sup>21</sup> Niels Bohr Institute, University of Copenhagen, Jagtvej 128, DK-2200 Copenhagen, Denmark
- <sup>22</sup> Institut d’Astrophysique de Paris, UMR 7095, CNRS, and Sorbonne Université, 98 bis boulevard Arago, F-75014 Paris, France
- <sup>23</sup> Jet Propulsion Laboratory, California Institute of Technology, 4800 Oak Grove Drive, Pasadena, CA 91001, USA
- <sup>24</sup> Department of Physics and Astronomy, UCLA, PAB 430 Portola Plaza, Box 951547, Los Angeles, CA 90095-1547, USA
- <sup>25</sup> Department of Astronomy and Astrophysics, University of California, Santa Cruz, 1156 High Street, Santa Cruz, CA 95064, USA
- <sup>26</sup> National Research Institute of Astronomy and Geophysics (NRIAG), Cairo, Egypt
- <sup>27</sup> University of Geneva, 24 rue du Général-Dufour, 1211 Genève 4, Switzerland
- <sup>28</sup> University of Massachusetts Amherst, 710 North Pleasant Street, Amherst, MA 01003-9305, USA